



NAG3-913

IN-32-CR

271792

P-48

Electromagnetic Properties of Material Coated Surfaces

L. Beard, J. Berrie, R. Burkholder,
A. Dominek, E. Walton and N. Wang

The Ohio State University
ElectroScience Laboratory

Department of Electrical Engineering
Columbus, Ohio 43212

Technical Report 720964-5
Grant ~~NAG3-913~~
NAG
October 1989

National Aeronautics and Space Administration
Lewis Research Center
Cleveland, OH 44135

(NASA-CR-186466) ELECTROMAGNETIC PROPERTIES
OF MATERIAL COATED SURFACES Annual Report
(Ohio State Univ.) 48 p CSCL 20N

N90-19466

Unclass

G3/32 0271792

NOTICES

When Government drawings, specifications, or other data are used for any purpose other than in connection with a definitely related Government procurement operation, the United States Government thereby incurs no responsibility nor any obligation whatsoever, and the fact that the Government may have formulated, furnished, or in any way supplied the said drawings, specifications, or other data, is not to be regarded by implication or otherwise as in any manner licensing the holder or any other person or corporation, or conveying any rights or permission to manufacture, use, or sell any patented invention that may in any way be related thereto.

REPORT DOCUMENTATION PAGE		1. REPORT NO.	2.	3. Recipient's Accession No.	
4. Title and Subtitle Electromagnetic Properties of Material Coated Surfaces				5. Report Date October 1989	
7. Author(s) L. Beard, J. Berrie, R. Burkholder A. Dominek, E. Walton, N. Wang				6. Performing Org. Rept. No. 720964-5	
9. Performing Organization Name and Address The Ohio State University ElectroScience Laboratory 1320 Kinnear Road Columbus, OH 43212				10. Project/Task/Work Unit No.	
				11. Contract(C) or Grant(G) No. (C) (G) NSG3-913	
12. Sponsoring Organization Name and Address National Aeronautics and Space Administration Lewis Research Center Cleveland, OH 44135				13. Report Type/Period Covered Annual Report	
				14.	
15. Supplementary Notes					
16. Abstract (Limit: 200 words)					
<p>The electromagnetic properties of material coated conducting surfaces have been investigated. The coating geometries consist of uniform layers over a planar surface, irregularly shaped formations near edges and randomly positioned, electrically small, irregularly shaped formations over a surface. Techniques to measure the scattered field and constitutive parameters from these geometries were studied. The significance of the scattered field from these geometries warrants further study.</p>					
17. Document Analysis a. Descriptors					
b. Identifiers/Open-Ended Terms					
c. COSATI Field/Group					
18. Availability Statement A Approved for public release; Distribution is unlimited.			19. Security Class (This Report) Unclassified		21. No. of Pages 46
			20. Security Class (This Page) Unclassified		22. Price



Contents

List of Figures	iv
1 Introduction	1
2 Near Field Scattering Measurements	3
I Experimental Configuration	3
II Near Field Cross Range Transformation	4
III Examples	6
IV Experimental Results	7
V Metal Sphere With Cross Range Processing	11
VI Background Stability Study	13
VII Equipment Performance Comparison	18
VIII Best Measurement Without Cross Range Processing	19
IX Further Theoretical Studies	21
3 Material Scattering	23
4 Material Parameter Determination	29
5 Conclusions	37

List of Figures

2.1	Top view of the metal chamber used in experiments.	4
2.2	Block diagram of microwave instrumentation.	5
2.3	Diagram of back projection algorithm geometry.	6
2.4	Amplitude vs. horizontal position for 3 theoretical scatterers (left) and geometry of experiment (right). Focussing on the nearest scatterer. (dot-dash line = line of computation; short-long dash line = location of chamber wall) Scan +2/-2 meters at 6 meters from targets. 10 GHz.	7
2.5	Amplitude vs. horizontal position for 3 theoretical scatterers (left) and geometry of experiment (right). Scan center scatterer. 10 GHz.	8
2.6	Amplitude vs. horizontal position for 3 theoretical scatterers (left) and geometry of experiment (right). 10 GHz.	9
2.7	Amplitude vs. horizontal position for 2 experimental scatterers (left) and geometry of experiment (right). Dot-dash line = line of computation; short-long dash line = location of chamber wall. Scan 0 to 1 meter at 3.66 meters from targets. 10 GHz.	10
2.8	Amplitude vs. horizontal position for 2 experimental scatterers (left) and geometry of experiment (right). 6 GHz. . .	11
2.9	Amplitude vs. horizontal position for 2 experimental scatterers (left) and geometry of experiment (right). 2 GHz. . .	12

2.10	Amplitude vs. horizontal position for a metal sphere (left) and geometry of experiment (right). Dot-dash line = line of computation; short-long dash line = location of chamber wall. Scan -0.8 to +0.2 meter at 3.05 meters from targets. 18 GHz.	13
2.11	Amplitude vs. horizontal position for a metal sphere (left) and geometry of experiment (right). 10 GHz.	14
2.12	Amplitude vs. horizontal position for a metal sphere (left) and geometry of experiment (right). 2 GHz.	15
2.13	Background reduction ratio versus time between subtracted measurements, from 2 to 18 GHz, for empty metal chamber (solid lines) and cables only (dashed lines).	16
2.14	Physical displacement corresponding to measured background reduction ratio after 30 minutes.	18
2.15	Required maximum physical displacement versus frequency to achieve a background reduction ratio of -20 dB.	19
2.16	Impulse response of a 3.2" diameter metal sphere obtained from frequency-scanned measurements taken with the radar from the ESL's compact range.	20
2.17	Impulse response of the metal sphere of previous figure measured with the HP 8510 system.	21
2.18	Best measurement of the RCS of a metal sphere without cross range processing (solid curve) and the theoretically exact RCS (dashed curve).	22
3.1	General material formation analyzed for electromagnetic scattering characteristics.	24
3.2	Material geometries used in scattering calculations.	26
3.3	RCS patterns at 10 GHz for TM_z excitation. Geometry A - solid line, geometry B - short dash line and no coating - long dash line. $\epsilon_r = 2.5$	27
3.4	RCS patterns at 10 GHz for TE_z excitation. Geometry A - solid line, geometry B - dashed line and no coating - long dash line. $\epsilon_r = 2.5$	28

4.1	Conceptual hardware configuration for surface wave measurements.	30
4.2	Analyzed geometry coatings for the dominant surface wave propagation constant.	32
4.3	The attenuation and phase constant for a single layered coating where $\epsilon_r = (2.54, -j0.)$ and $t = .125''$ (negligible attenuation).	33
4.4	The attenuation and phase constant for a double layered coating where $\epsilon_{r1} = (30., -j5.)$, $\epsilon_{r2} = (2.54, -j0.)$, $t_1 = .125''$ and $t_2 = .015625''$	34
4.5	The attenuation and phase constant for a double layered coating where $\epsilon_{r1} = (30., -j5.)$, $\epsilon_{r2} = (2.54, -j0.)$, $t_1 = .015625''$ and $t_2 = .125''$	35

Chapter 1

Introduction

The presence of material coatings on surfaces is not uncommon. Such coatings have a definite influence on the electromagnetic scattering performance of these surfaces which are often perfectly conducting. The coatings of interest have several exterior contours which do not necessarily conform to the surface contour. The research reported here is from the first year of a two year study. The goal of this work is to develop a measurement technique and hardware to obtain:

- the electrical parameters of particular dielectric coatings,
- the scattered field characteristics due to these dielectric coatings,
- the measurement of the scattered field from these dielectric coatings in a metal chamber.

Scattered field measurements are commonly performed in specially designed rooms with the appropriate instrumentation radar. The conditions imposed upon acquiring the scattering performance for the material coatings of interest do not allow the use of conventional techniques. These measurements have to be performed in a chamber with metal walls which allow

contamination of the desired signal with multiple bounce terms. Chapter 2 discusses this technique in detail in terms of the required hardware, the error terms in the measurement, and the signal processing used to minimize the effect of these error terms.

Any measurement program should have an adjoining analytical program not only to confirm the measured results but also to provide an understanding of the physics involved in the scattering problem. Three generic surfaces have been studied and measurements have been taken to confirm the analytical approximations made for one surface type as presented in Chapter 3.

The final area of effort has been to develop a technique to determine the actual effective electrical parameters for material coatings of interest. Conventional techniques are not appropriate for materials formed in a thin "planar" layer. The technique under development, as discussed in Chapter 4, incorporates the behavior of surface waves on coated surfaces to obtain the electrical parameters of the material.

Chapter 2

Near Field Scattering Measurements

It is often necessary to measure the radar cross section (RCS) of a scatterer in a non-ideal environment. There are often space restrictions and undesired objects (clutter) in the neighborhood of the target. To simulate a non-ideal environment, measurements can be made inside a metal chamber. This chapter discusses a set of experiments carried out at the ESL in a metal chamber 7.3 meters long, 1.83 meters high, and 2.74 meters wide.

I Experimental Configuration

As shown in Figure 2.1, the ends of the chamber were open, with an antenna positioner at one end and a cinder block wall 0.2 meters beyond the other end. Using computer control, a pair of wide band horn antennas could be moved horizontally across the open end of the chamber. As shown in Figure 2.2, the instrumentation consisted of an antenna positioner, a Hewlett-Packard 8510 network analyzer, a synthesized microwave source, and a pair of high speed microwave switches (used for hardware range gating) and their associated controller. The potential frequency band for

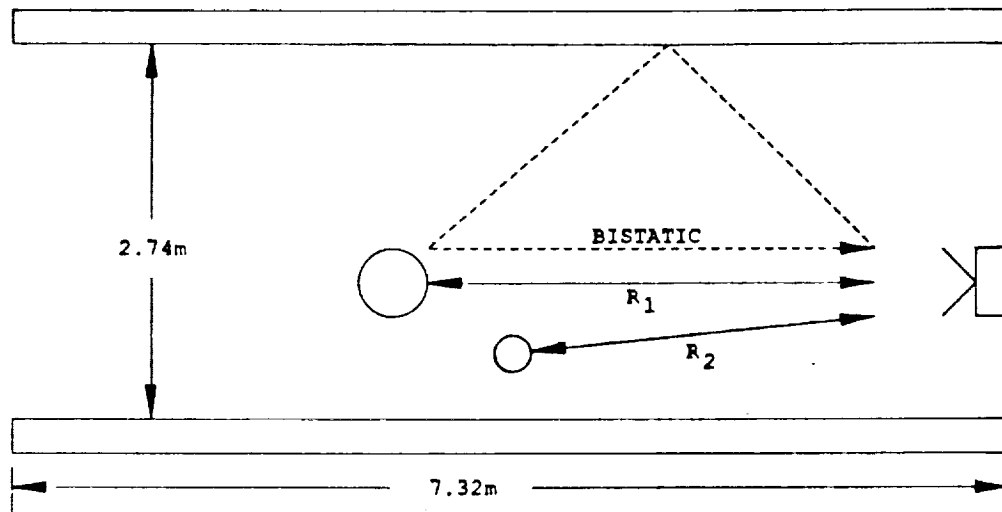


Figure 2.1: Top view of the metal chamber used in experiments.

the measurements was from 2 to 18 GHz.

II Near Field Cross Range Transformation

Radar scattering data was measured as a function of frequency at each of a number of locations along the horizontal scan length available for the wide band horns. The system was calibrated using similar measurements for both the empty chamber and the chamber with only a known sphere installed.

The data could have been transformed to the angle (or cross range) domain using a classical Fourier transformation if the aperture of the scan and the size of the target set had both been in the far field. Since they were not, a near field back projection algorithm was used [1,2]. As shown in Figure 2.3, the algorithm considers that the area of interest is a line located at a specific distance from the scan aperture.

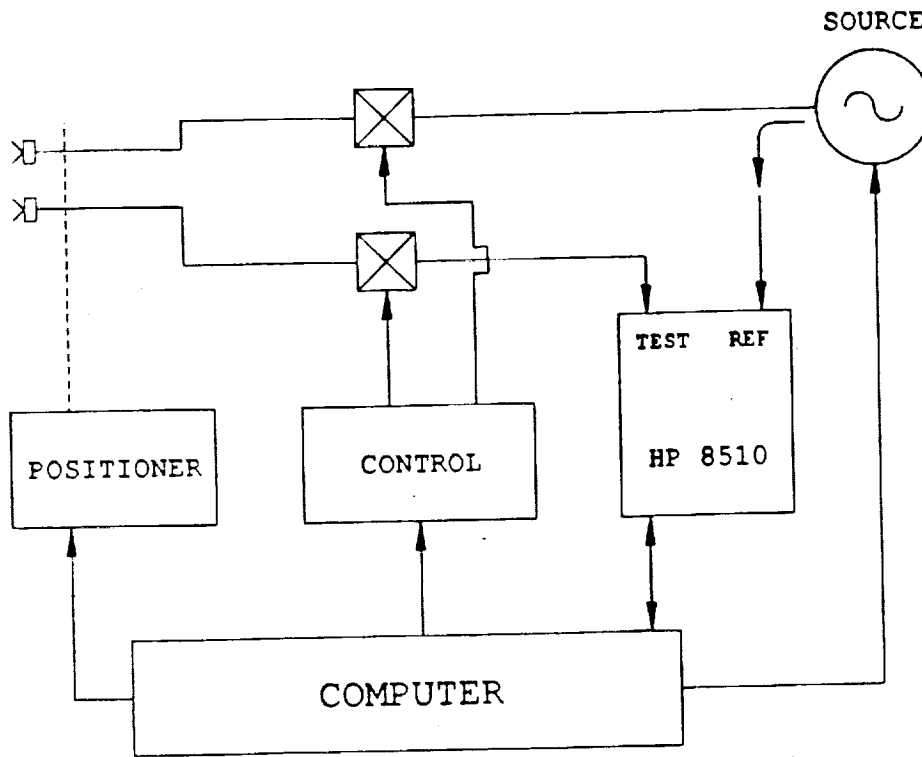


Figure 2.2: Block diagram of microwave instrumentation.

The line is broken up into segments and the signal originating from each particular segment is estimated by computing backward to this element from each of the observation points. The signal originating from the n^{th} cell is computed as

$$E_n = \frac{1}{M} \sum_{m=1}^M \left(\frac{R_{mn}}{R_0} \right)^2 S_m e^{jk2R_{mn}} \quad (2.1)$$

where

E_n is the signal radiating from cell n

S_m is the signal measured at the m^{th} horizontal position

R_{mn} is the distance from the m^{th} measurement point to the n^{th} cell

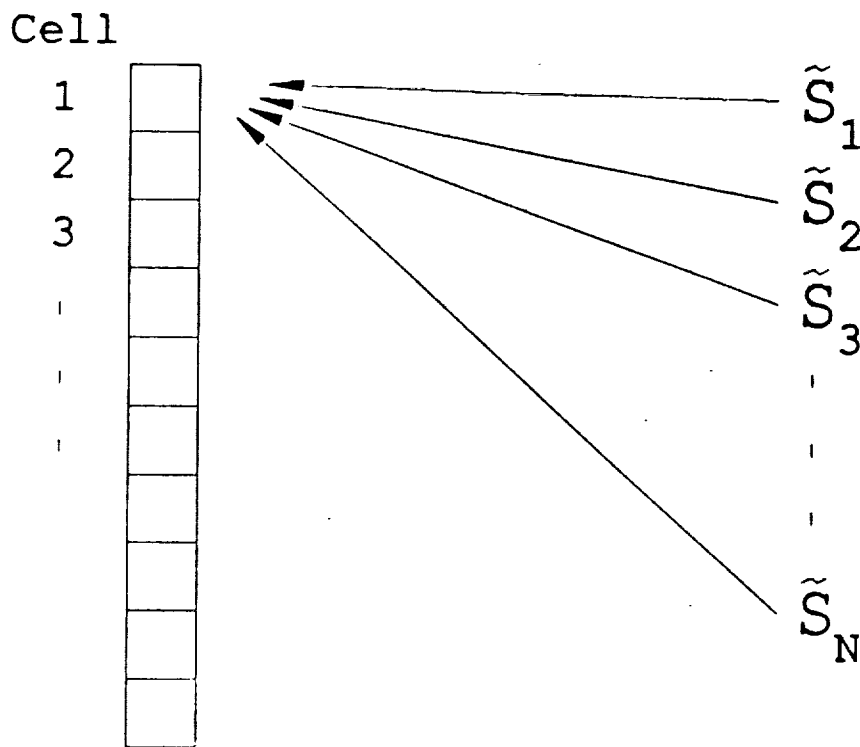


Figure 2.3: Diagram of back projection algorithm geometry.

R_0 is the distance to calibration reference

$$k = 2\pi/\lambda$$

III Examples

An example of the application of this equation is shown in Figure 2.4. For this figure, three ideal point scatterers with amplitudes and locations as shown on the figure were used. A chamber wall was located at 3 meters from the center (short-long dashed line). The amplitude of the cells as a function of horizontal position is shown in the left hand plot. In this plot, it can be seen that the sharpest response comes from the scatterer closest to

the line of computation (the dot-dash line in the right hand diagram). The farther the scatterer is from the computation line, the more out of focus and off position it becomes. This can be described as throwing a fuzzy shadow on the line of computation. Note also the image response at approximately +3 meters in the amplitude plot. This is a result of reflections from the wall. Similar plots are shown in Figure 2.5 (focused on the middle scattering point) and Figure 2.6 (focused on the farthest scattering point). Note the defocussing and shift in location of the response from points not near the line of computation.

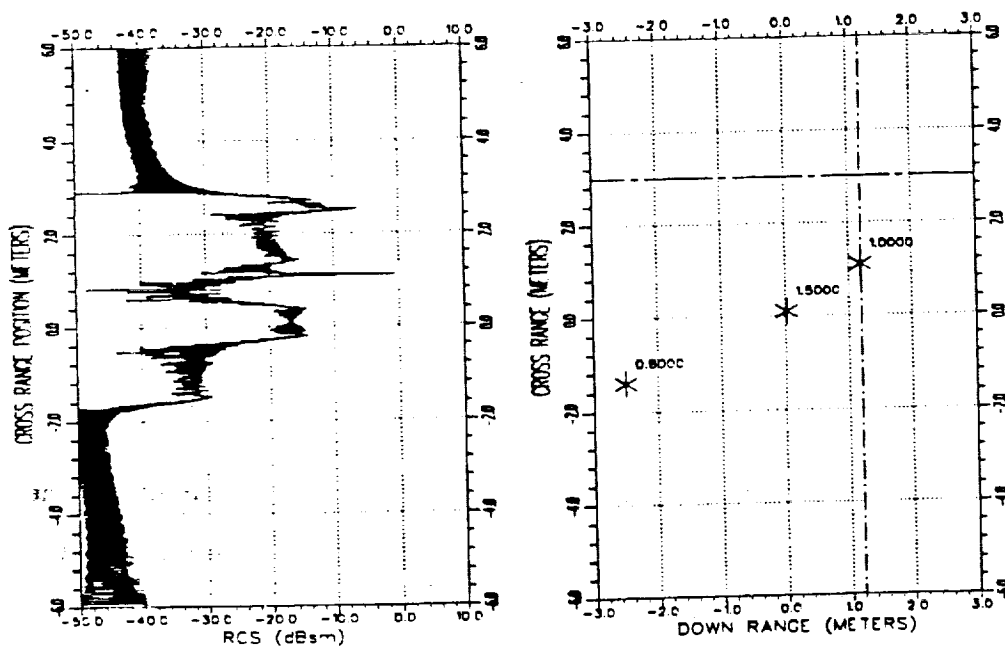


Figure 2.4: Amplitude vs. horizontal position for 3 theoretical scatterers (left) and geometry of experiment (right). Focussing on the nearest scatterer. (dot-dash line = line of computation; short-long dash line = location of chamber wall) Scan +2/-2 meters at 6 meters from targets. 10 GHz.

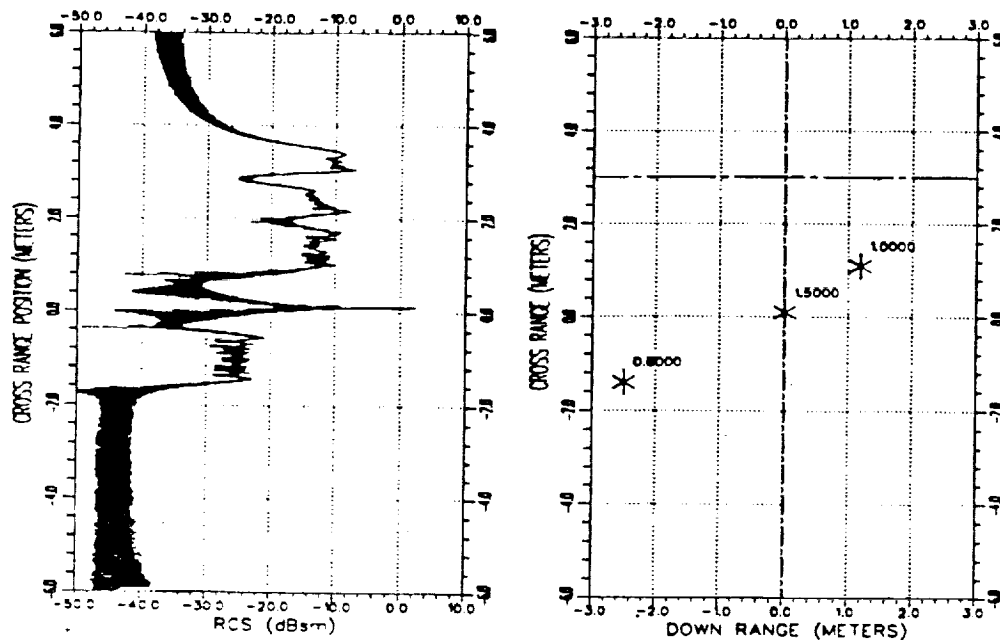


Figure 2.5: Amplitude vs. horizontal position for 3 theoretical scatterers (left) and geometry of experiment (right). Scan center scatterer. 10 GHz.

IV Experimental Results

An experimental test of these concepts was performed in the chamber. The target set in this case was a pair of trihedrals located 3.66 meters from the feed support. They were separated horizontally by 33 cm and in range by 30 cm (approximately) as shown in the right hand drawing of Figure 2.7. They were supported vertically by an obliquely oriented ogival styrofoam column.

In this case, a set of measurements was made in which the scattering from the target set was measured as a function of frequency from 2 to 10 GHz. The antenna moved from the center of the chamber to a distance of 1 meter to the right of center in 1 cm steps, for a total of 101 positions.

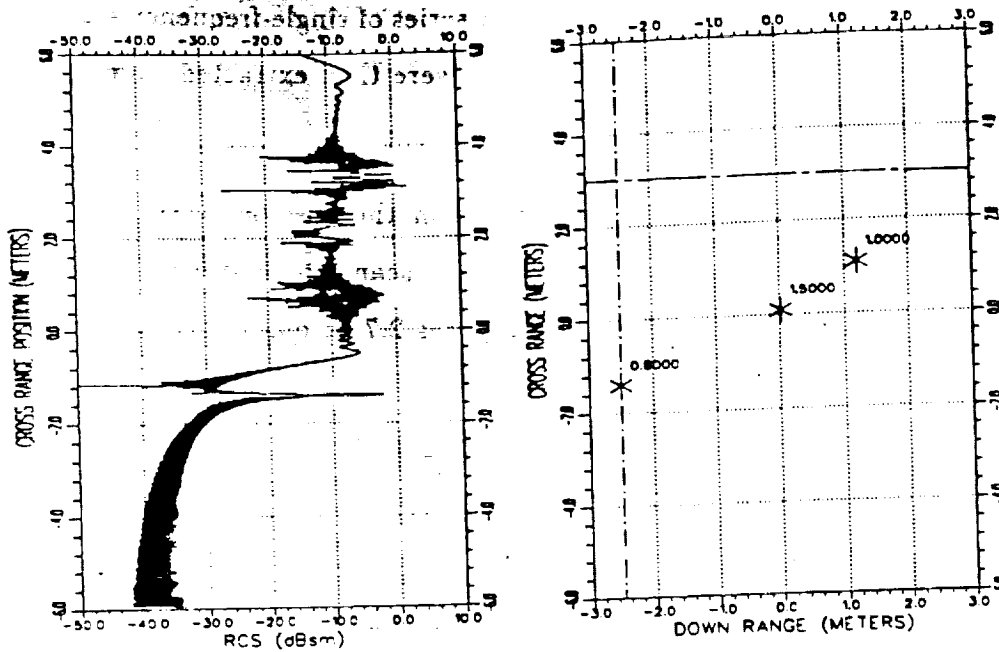


Figure 2.6: Amplitude vs. horizontal position for 3 theoretical scatterers (left) and geometry of experiment (right). 10 GHz.

The data was calibrated as shown in the equation below [3]

$$C_j = \frac{S_t - S_b}{S_r - S_b} S_e \quad (2.2)$$

where

C_j calibrated RCS in DBSM

S_t target data

S_b empty chamber (background) data

S_r reference data (smaller trihedral)

S_e exact data $\sigma = \frac{4\pi A^2}{\lambda^2}$ (Note that this is really only a high freq. approximation.)

The results were range gated using Fourier transform techniques to exclude horn coupling and back wall effects. A series of single-frequency scans (ie: horizontal position scans on the target) were then extracted from the data.

The back projection algorithm described in the previous section was then used to transform these single frequency scans to scattering versus position plots. The results are shown in Figures 2.7 through 2.9.

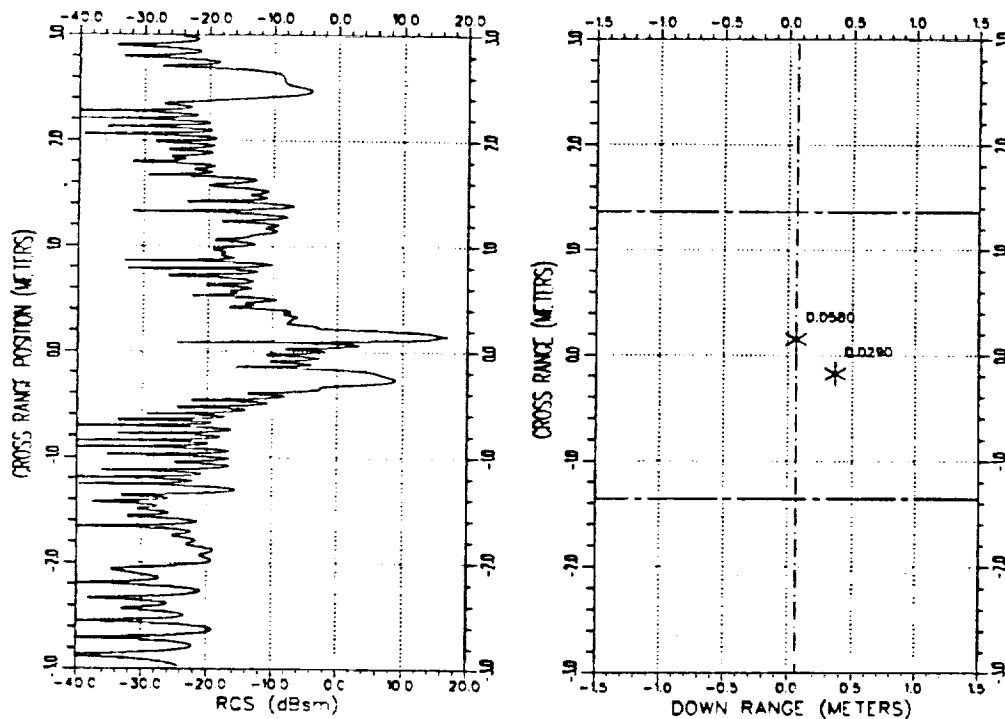


Figure 2.7: Amplitude vs. horizontal position for 2 experimental scatterers (left) and geometry of experiment (right). Dot-dash line = line of computation; short-long dash line = location of chamber wall. Scan 0 to 1 meter at 3.66 meters from targets. 10 GHz.

The walls of the chamber are shown on these figures, as well as the line of computation for the scattering amplitude versus position. Note that

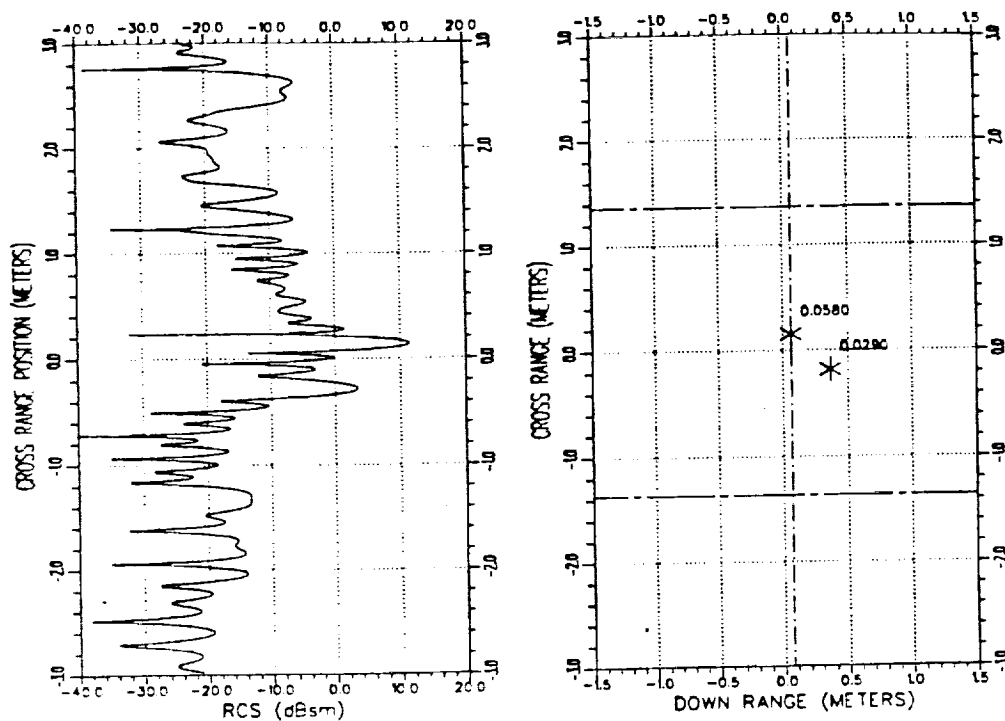


Figure 2.8: Amplitude vs. horizontal position for 2 experimental scatterers (left) and geometry of experiment (right). 6 GHz.

as the frequency varies from 10 GHz to 6 GHz then to 2 GHz, that the resolution of the responses decreases. The effect of side lobes can also be seen, especially in Figure 2.8. As experiments proceed to targets with greater bistatic scattering terms and smaller RCS values, the resolution and sidelobe suppression characteristics of this signal processing technique will become more important. Windowing techniques common in classical far-field FFT analysis will be developed for this data to further suppress the sidelobes.

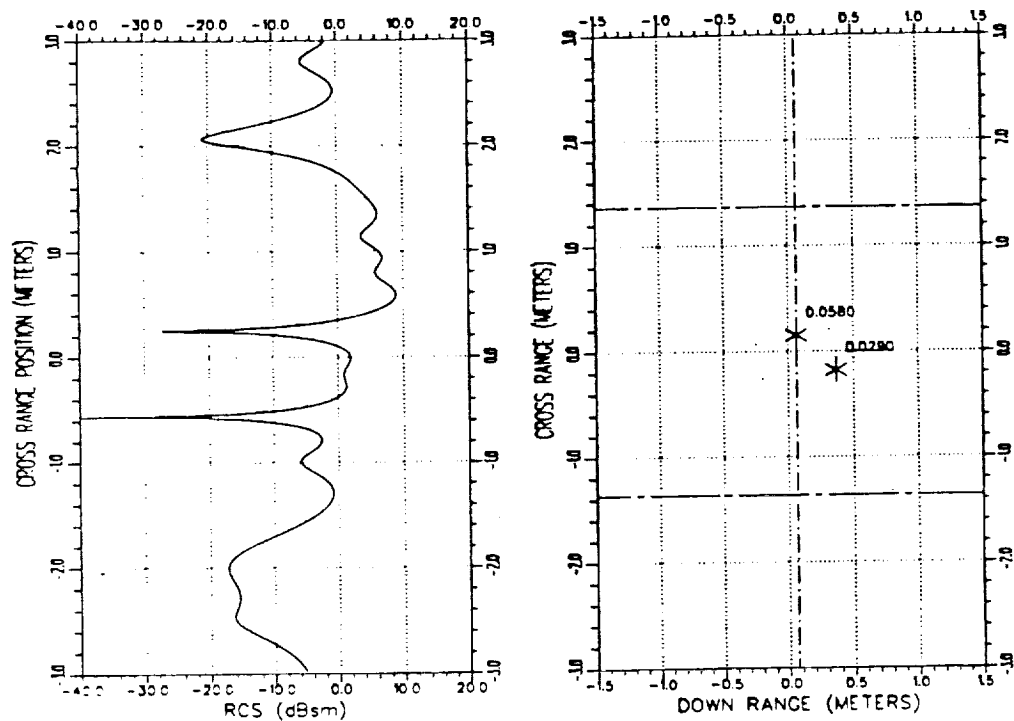


Figure 2.9: Amplitude vs. horizontal position for 2 experimental scatterers (left) and geometry of experiment (right). 2 GHz.

V Metal Sphere With Cross Range Processing

For this study, measurements of a 6 inch diameter metal sphere in the chamber were made with a scanning probe. The probe again moved 1 meter in 1 centimeter increments. At each probe position a frequency scan was made from 2 to 18 GHz in 0.5 GHz increments. The sphere was 10 feet from the probe. A hardware range gate was used with a pulse width of 6 nsec in order to remove the direct horn coupling.

The back-projection algorithm was performed on the data to obtain crossrange resolution. No background subtraction or software time gating

was used. In Figures 2.10 through 2.12 results for three frequencies show that the sphere return was approximately 10 dB above the background level. A decrease in crossrange resolution with decreasing frequency is seen. Figure 2.11 shows peaks at approximately 2.8 meters on each side of the sphere which are due to images of the sphere in the side walls. Calculations indicate that a bistatic signal path (horn-wall-sphere-horn), as shown in Figure 2.1 (dashed line), should produce a broad peak at the location of the reflecting wall. This can be seen in Figure 2.11 at approximately -1.3 meters.

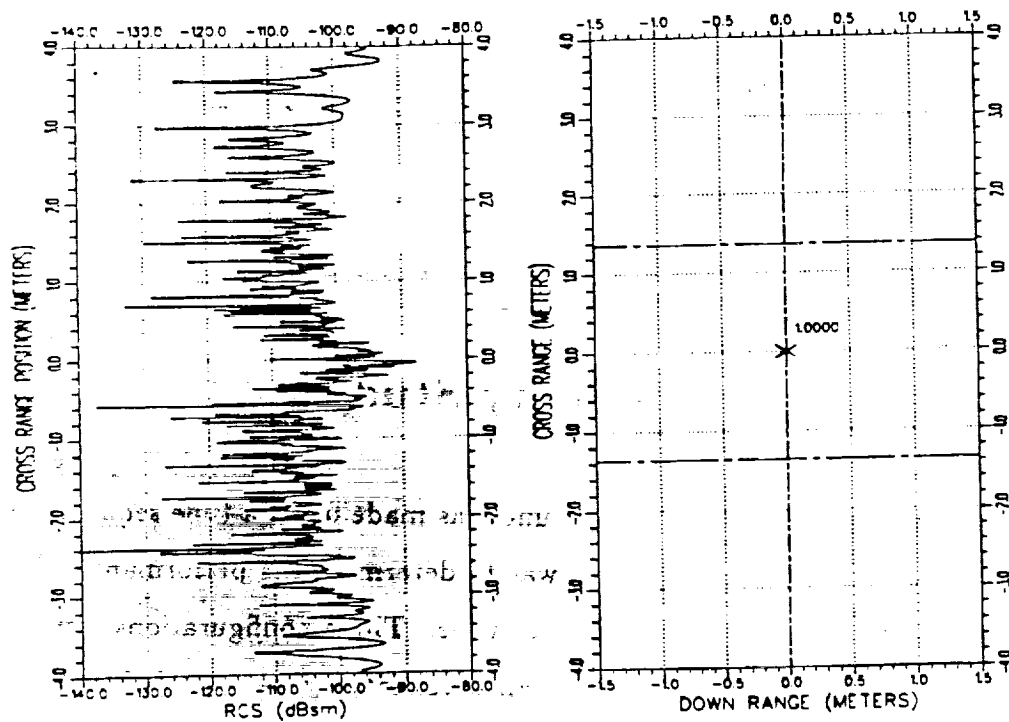


Figure 2.10: Amplitude vs. horizontal position for a metal sphere (left) and geometry of experiment (right). Dot-dash line = line of computation; short-long dash line = location of chamber wall. Scan -0.8 to +0.2 meter at 3.05 meters from targets. 18 GHz.

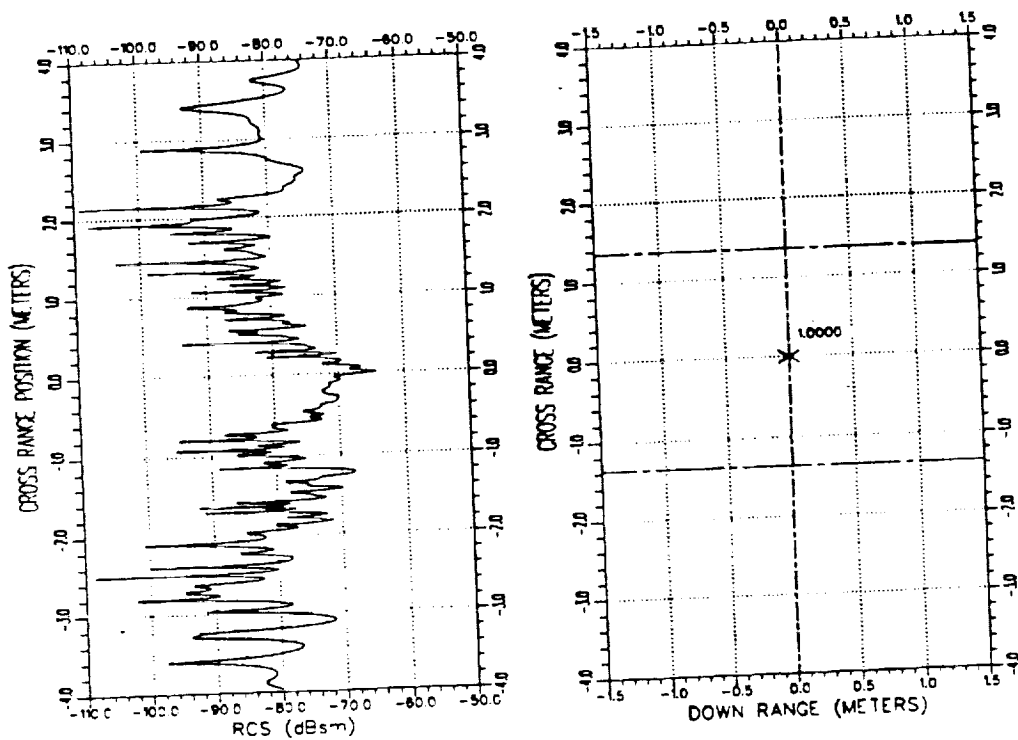


Figure 2.11: Amplitude vs. horizontal position for a metal sphere (left) and geometry of experiment (right). 10 GHz.

VI Background Stability Study

A study of the stability of the background was made using a time sequence of experimental measurements. This was to determine the performance of background subtraction as a function of time. Three configurations were used. First, a 2 foot long cable and an attenuator were installed, thus isolating the system from the antennas and the metal chamber. Second, the 2 foot cable was replaced by a 30 foot long cable. In the third configuration the hardware range gate and antennas were connected and installed in the empty metal chamber. The hardware range gate was set for a pulse width of 6 nsec and centered on the target zone 11 feet downrange. It was not

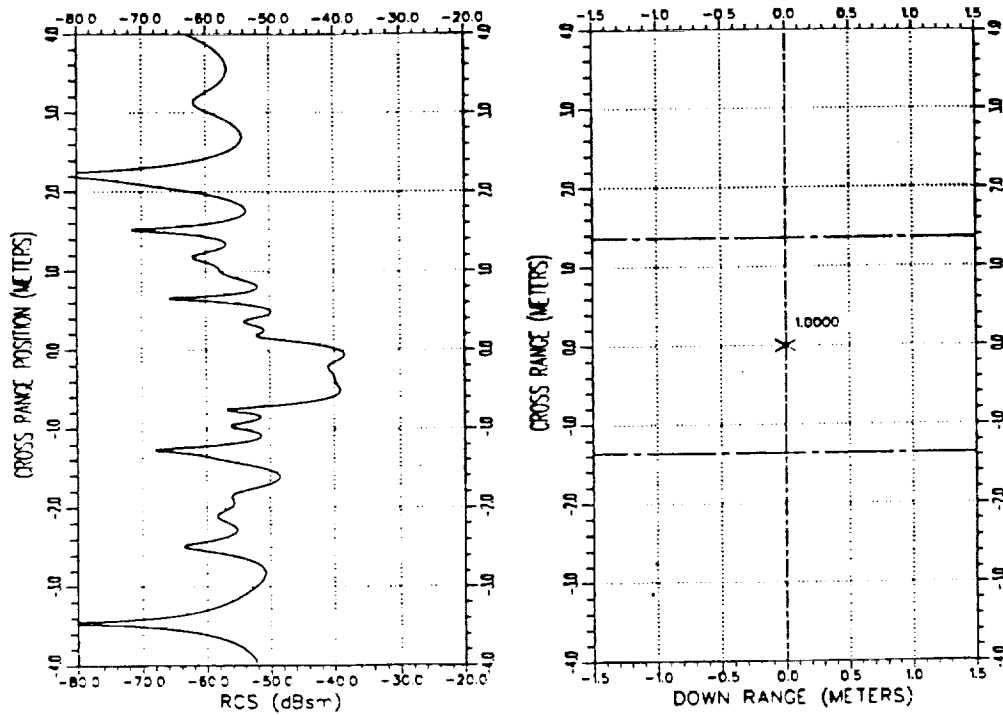


Figure 2.12: Amplitude vs. horizontal position for a metal sphere (left) and geometry of experiment (right). 2 GHz.

used in the first two configurations.

Figure 2.13 shows the results of the measurements in terms of what shall be referred to as the background reduction ratio. The background reduction ratio is obtained from the following equation

$$R(f_k) = \frac{S(f_k)_{\text{later}} - S(f_k)_{\text{earlier}}}{S(f_k)_{\text{earlier}}} \quad (2.3)$$

where

$R(f_k)$ is the background reduction ratio at frequency f_k

$S(f_k)_i$ is a background measurement at time i .

It is the ratio of the background level with subtraction to that without subtraction. It is plotted versus the elapsed time between measurements. Due to high variability of the data, the numbers used in these computations were obtained from approximate estimates of the typical values.

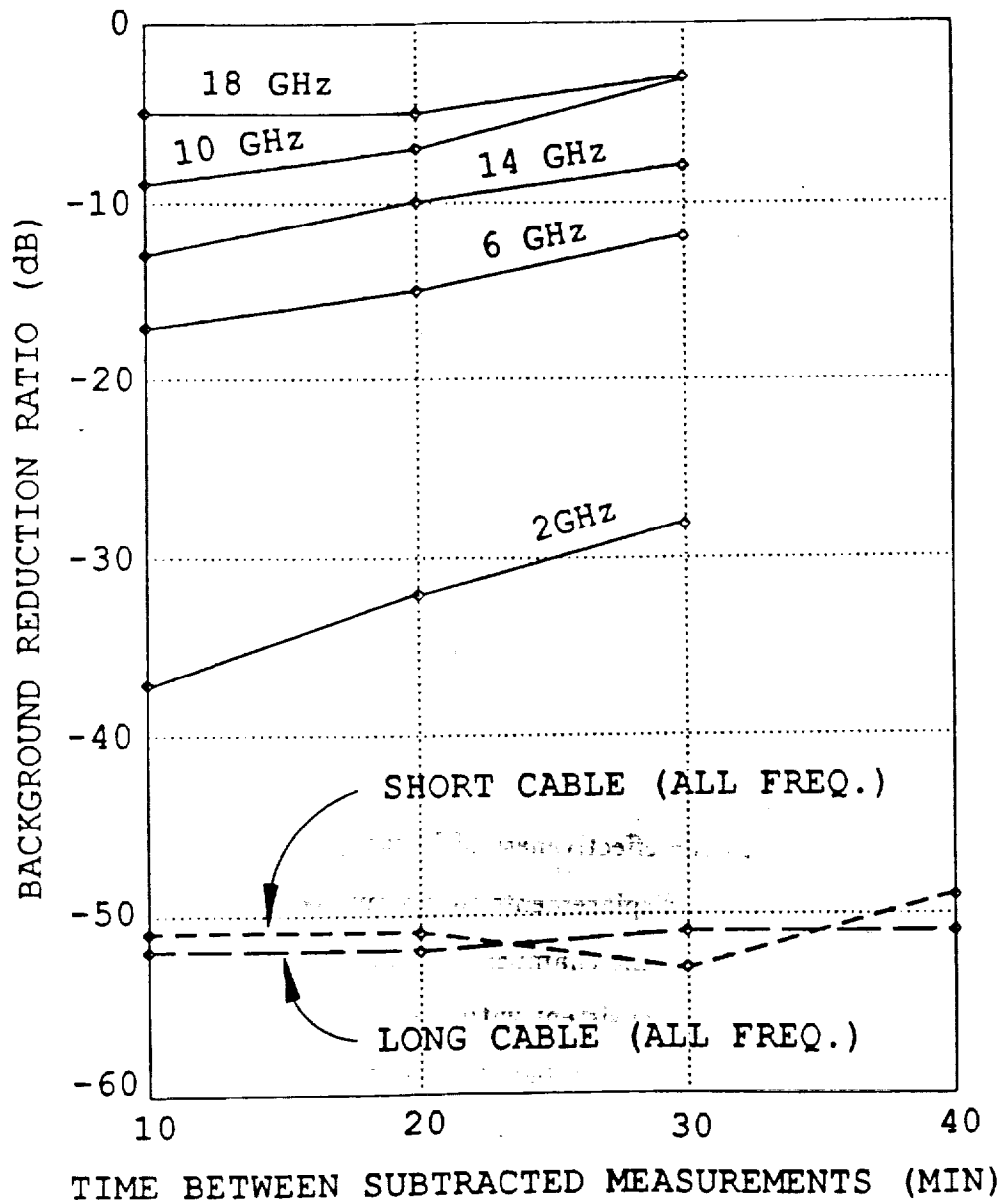


Figure 2.13: Background reduction ratio versus time between subtracted measurements, from 2 to 18 GHz, for empty metal chamber (solid lines) and cables only (dashed lines).

Frequency drift in the radar signal degrades the performance of background subtraction by causing the wavelengths in the two subtracted measurements to be different, thus adding error to the phase of the received signal which cannot be subtracted out. Frequency drift can be monitored by comparing the background reduction ratio for short and long cables since the phase variation depends upon the distance that the signal travels. The figure shows that the background reduction ratio was not degraded when changing from a short to a long cable, indicating that frequency drift is not the dominant factor affecting the performance of background subtraction. The figure also shows that for these two configurations, the performance remained relatively constant up to 40 minutes, which was the greatest time separation in this test.

When the hardware range gate and antennas were connected and exposed to the metal chamber, the background was reduced by at most 37 dB at 2 GHz after 10 minutes and as little as 3 dB at 18 GHz after 30 minutes. This degradation can be due to instabilities in the hardware range gate or physical movement of the metal chamber and the antenna along the line of sight. Clearly, the physical stability of both the background objects and the antenna is important to the effectiveness of background subtraction. Figure 2.14 shows the physical displacements that would cause the background reduction ratios measured in the chamber after 30 minutes. Displacements of approximately 1 mm are consistent with these data over the entire 2-18 GHz range. In order to maintain a background reduction ratio of -20 dB, the physical displacements listed in Figure 2.15 are the maximum allowable.

FREQ. GHZ	MEASURED BACKGROUND REDUCTION RATIO	CORRESPONDING PHYSICAL DISPLACEMENT
2	-28dB	0.48mm
6	-12dB	1.00mm
10	-3dB	1.73mm
14	-8dB	0.68mm
18	-3dB	0.96mm

Figure 2.14: Physical displacement corresponding to measured background reduction ratio after 30 minutes.

VII Equipment Performance Comparison

In this section a comparison is made between measurements taken with the HP 8510 system and an instrumentation system developed and refined for use in the ESL's compact range [3]. This system and the HP 8510 system were both used to make measurements of a 3.2 inch diameter metal sphere calibrated to a 6 inch diameter metal sphere from 6 feet away. Both systems used their own hardware range gates and the same dual ridge high gain horn antenna to transmit and receive. The HP 8510 system was set up as in Figure 2.2 except that the two antennas were replaced by one antenna connected to the input of a -3dB directional coupler. The results shown in

FREQ. GHZ	DESIRED BACKGROUND REDUCTION RATIO	REQUIRED MAX. DISPLACEMENT
2	-20dB	1.19mm
6	-20dB	0.40mm
10	-20dB	0.24mm
14	-20dB	0.17mm
18	-20dB	0.13mm

Figure 2.15: Required maximum physical displacement versus frequency to achieve a background reduction ratio of -20 dB.

Figure 2.16 for the compact range radar and Figure 2.17 for the HP 8510 system include software time gating specific to the calibration and target spheres.

VIII Best Measurement Without Cross Range Processing

In an effort to obtain the best possible (ie: a performance baseline) measurement without cross range processing, experiments were conducted with the antenna held stationary. Various amounts of absorber material were

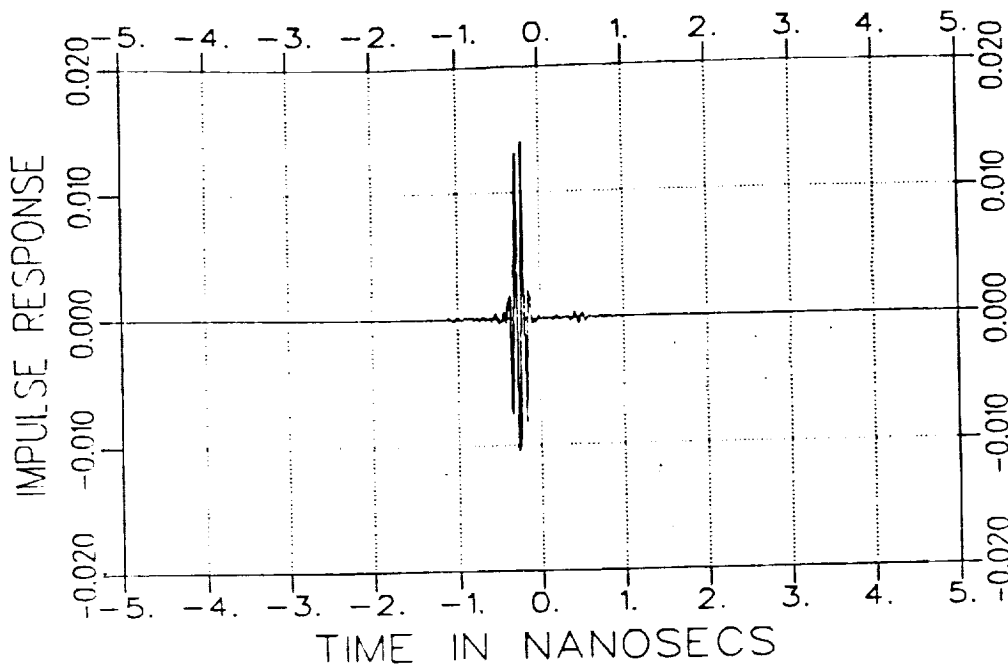


Figure 2.16: Impulse response of a 3.2" diameter metal sphere obtained from frequency-scanned measurements taken with the radar from the ESL's compact range.

placed on the walls of the chamber to reduce reflections and thereby improve the measurements. Hardware and software range gating were used to remove all signals due to scatterers that were not at the range of the targets. The most correct measurement of a 3 inch diameter metal sphere calibrated to a 6 inch diameter metal sphere was obtained with the floor covered with absorber and the other walls left bare. The antenna and target were positioned 2.5 feet above the floor and 6 feet apart. By placing the antenna and target closer to the absorber-covered floor than to the bare ceiling, the reflection in the ceiling was separated in time from the direct signal, thus allowing the direct signal to be isolated in software. Figure 2.18 shows that the measured RCS is generally within 1 dB of the exact theoretical RCS plotted over it with a dashed line. Adding absorber to the

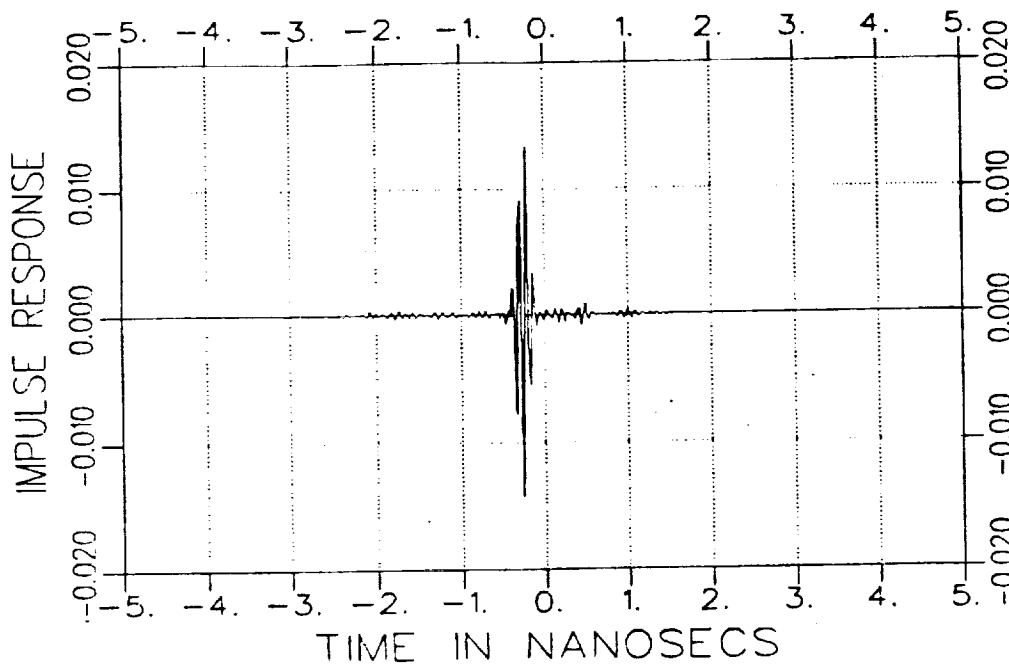


Figure 2.17: Impulse response of the metal sphere of previous figure measured with the HP 8510 system.

other walls did not improve the results.

IX Further Theoretical Studies

Present work now includes theoretical studies of two dimensional scan paths for the probe. A circular scan path is currently being simulated to determine its performance and the effects of the scan parameters. The advantage of a two dimensional scan path over a linear scan path is that it will allow separation of signals from scatterers in two dimensions, whereas a linear scan path does not allow scatterers arranged perpendicular to it to be resolved.

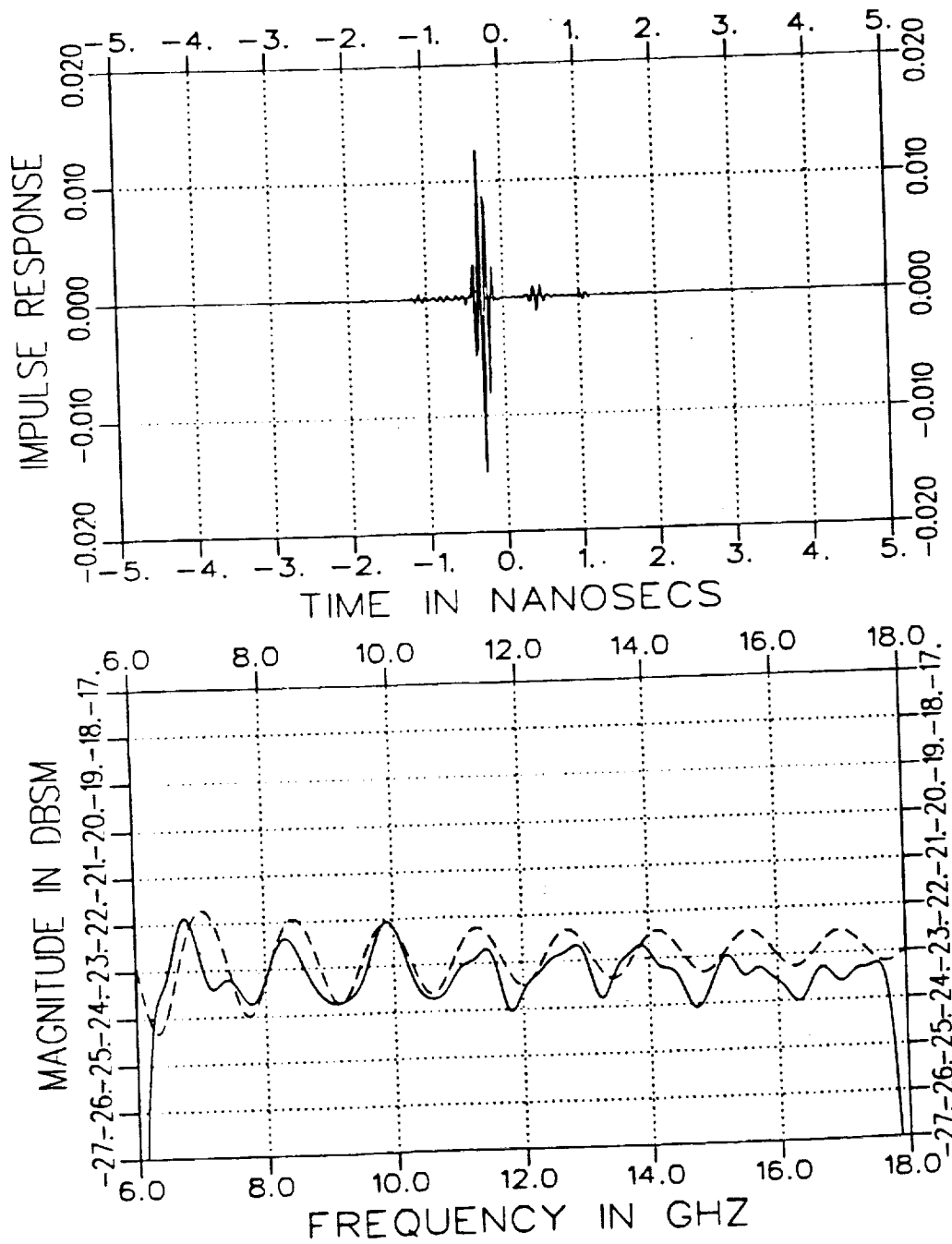


Figure 2.18: Best measurement of the RCS of a metal sphere without cross range processing (solid curve) and the theoretically exact RCS (dashed curve).

Chapter 3

Material Scattering

Three general coatings have been analyzed with available user software (FORTRAN based) and user manuals [4,5]. Figure 3.1 illustrates the two and three dimensional geometries. These geometries can be classified into two general types, i.e., rough surface (thin coating) and bulk formation of material in localized areas.

The scattering from the rough surface coatings has been analyzed from two different approaches. The appropriate analysis is dependent upon how well the model matches the actual geometry. One analysis [4] models surface roughness as a two dimensional sinusoidal undulating surface which uses Physical Optics (PO). The results from this indicate the potential effect of a grating lobe in the scattered field. The presence of a grating lobe dramatically increases the scattered field when the surface periodicity for a given look angle forms scattering centers located an integral number of half wavelengths apart. The physical explanation of this behavior is that the scattered fields will all add in phase when the total path length to similar portions of the surface (scattering centers) are multiples of one wavelength. Grating lobe phenomena can occur in several scattering situations and can be a dominant backscatter mechanism [6].

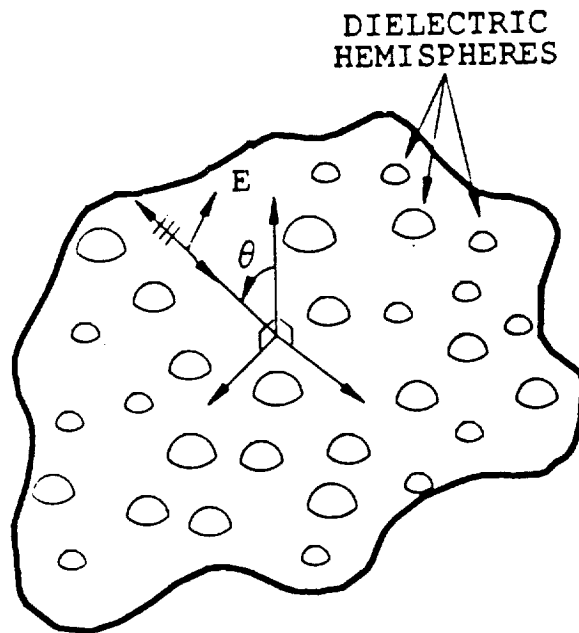
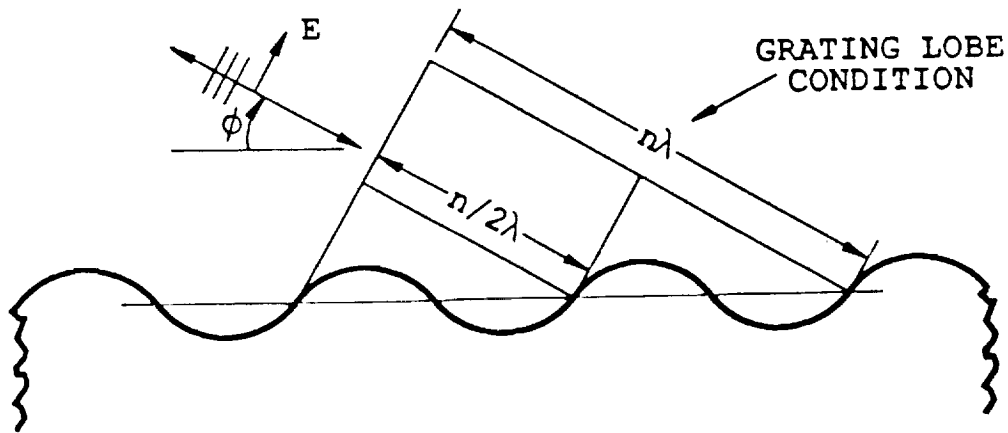


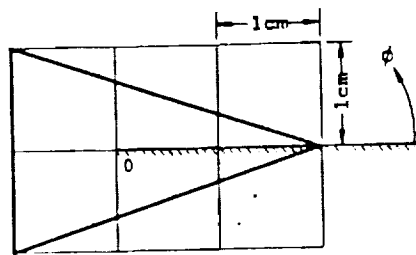
Figure 3.1: General material formation analyzed for electromagnetic scattering characteristics.

This scattered field effect due to periodicity is also shown in the other rough surface model which is a three dimensional model [5]. This model incorporates the scattering from electrically small dielectric hemispheres over a conducting planar groundplane. The geometries which the developed code can accommodate are rectangular patches and periodically arrayed strips. These basic geometries can also be paired to simulate the leading edges of swept back wings.

The last model investigated has the material coating in a bulk, localized formation on the edge of a conducting half plane. Figures 3.3 and 3.4 illustrate the backscattered fields for both principle incident polarizations for the geometries shown in Figures 3.2 at 10 GHz and a relative dielectric constant of $\epsilon_r = 2.5$. These results demonstrate a definite material influence on the scattered field for a thin conducting surface, especially when the electric field is polarized in the plane of incidence. These results are for a two dimensional geometry. A three dimensional value can be obtained when the incidence plane is normal to the edge of length L by multiplying the two dimensional value by $2\frac{L^2}{\lambda}$.

Presently, a code is being developed to analyze material coatings on "thick" conducting surfaces which have non-zero cross sectional area.

Geometry A



Geometry B

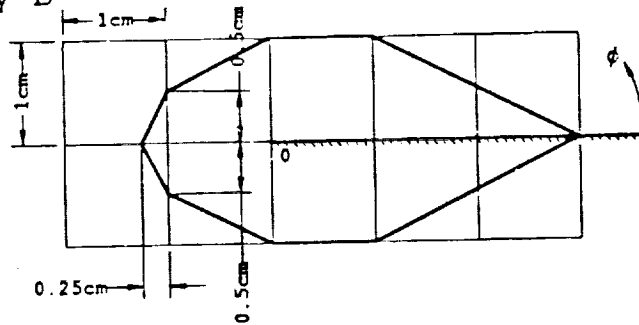


Figure 3.2: Material geometries used in scattering calculations.

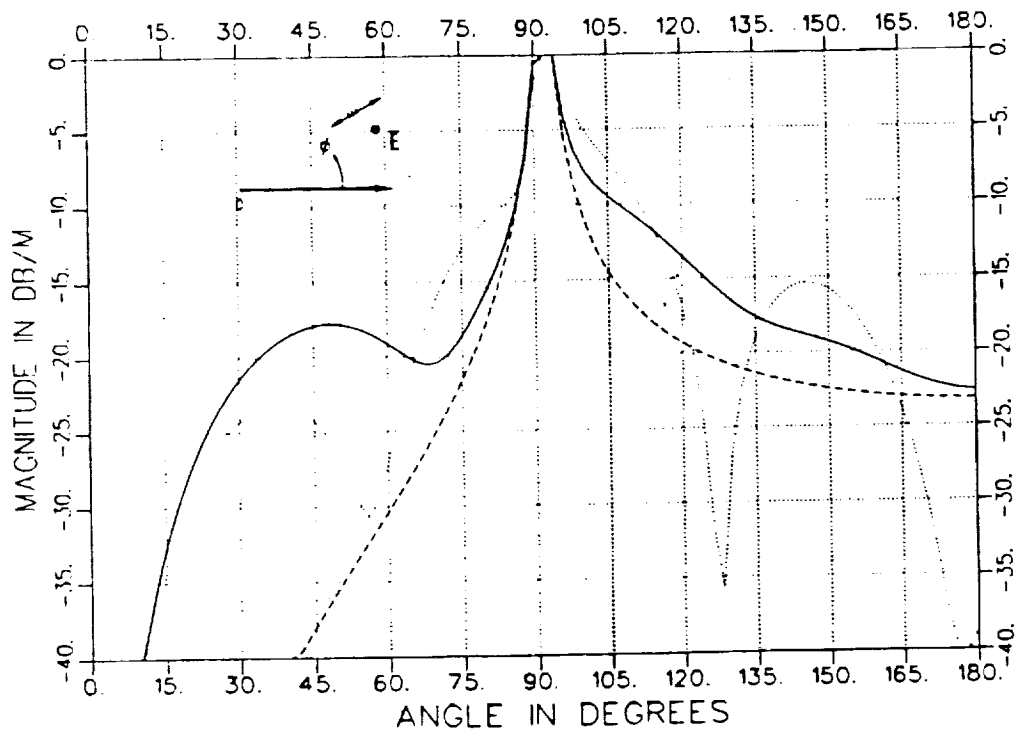


Figure 3.3: RCS patterns at 10 GHz for TM, excitation. Geometry A - solid line, geometry B - short dash line and no coating - long dash line. $\epsilon_r = 2.5$

ORIGINAL PAGE IS
OF POOR QUALITY

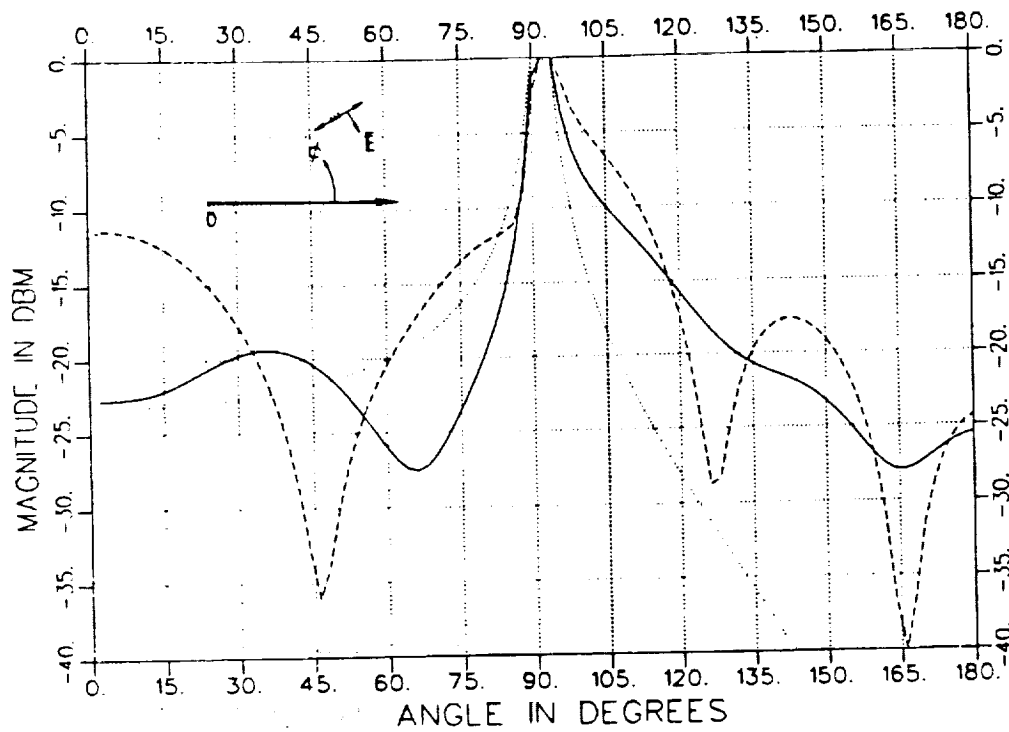


Figure 3.4: RCS patterns at 10 GHz for TE₂ excitation. Geometry A - solid line, geometry B - dashed line and no coating - long dash line. $\epsilon_r = 2.5$

ORIGINAL PAGE IS
OF POOR QUALITY

Chapter 4

Material Parameter Determination

A novel technique is under development to obtain the complex dielectric constant (ϵ) for a material coating on a conducting groundplane. The technique uses the field behavior of surface waves of coated surfaces. Figure 4.1 conceptually illustrates the geometry which entails the use of two probes to measure the transmitted field from one probe to another. The electric field coupling between the probes can be expressed as

$$E_z = \frac{A}{\sqrt{\rho}} e^{-\gamma(\epsilon)\rho} \quad (4.1)$$

when ρ is electrically large ($\geq 5\lambda$). The desired parameter is the propagation constant $\gamma = \alpha + j\beta$ which is a function of the dielectric constant, ϵ .

The proper dielectric constant can be found through a standard Newton-Raphson iteration scheme on the following functional

$$F = \gamma_{cal} - \gamma_{meas} \quad (4.2)$$

where subscripts "cal" and "meas" denote calculated and measured propagation constants. The iteration drives the functional to zero and yields the proper value of ϵ .

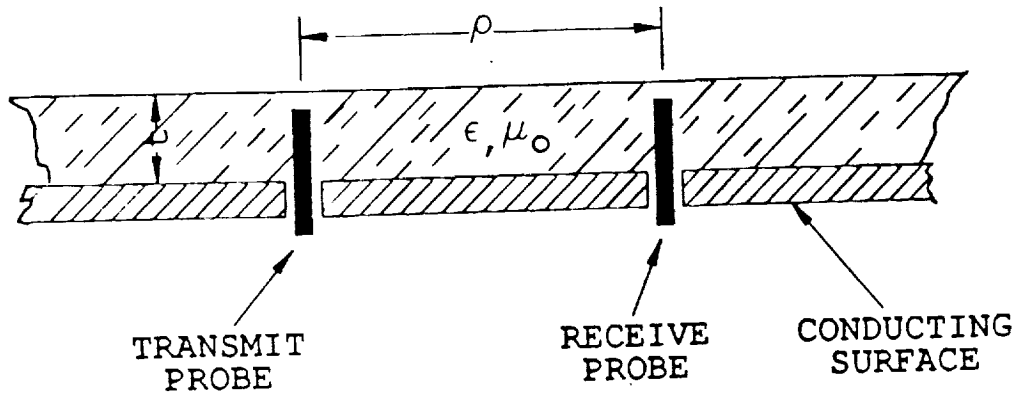


Figure 4.1: Conceptual hardware configuration for surface wave measurements.

This constant can be experimentally determined by taking two measurements at different distances to eliminate the unknown constant A . The final equation is

$$\gamma = -\frac{1}{\rho_1 - \rho_2} \ln \left\{ \frac{\sqrt{\rho_1} E_x(\rho_1)}{\sqrt{\rho_2} E_x(\rho_2)} \right\}. \quad (4.3)$$

The measurements to obtain E_x can readily be performed with a network analyzer such as the HP 8510.

The propagation constant can be analytically determined for a uniform, homogenous layer of material of thickness t over a conducting surface. Figure 4.2 illustrates two geometry coatings which have been studied. Each coating has a transcendental equation which can be solved for γ using a Newton-Raphson search algorithm. Each equation has several roots (γ 's) of which the one with the lowest attenuation constant (α) is the one of interest. The transcendental equation for a single layer is [7]

$$u \tan ut = \frac{\epsilon_1}{\epsilon_0} v \quad (4.4)$$

where $-v^2 - \gamma^2 = k_0^2$ and $u^2 - \gamma^2 = k_1^2$. The corresponding expression for

a double layer is [8]

$$A_1 A_2 = A_3 A_4 \quad (4.5)$$

where

$$A_1 = \left[\frac{v\epsilon_1}{u_1\epsilon_0} - \tan u_1(t_1 + t_2) \right], \quad (4.6)$$

$$A_2 = \left[\frac{u_2\epsilon_1}{u_1\epsilon_2} \tan u_2 t_2 \tan u_1 t_2 + 1 \right], \quad (4.7)$$

$$A_3 = \left[\frac{v\epsilon_1}{u_1\epsilon_0} \tan u_1(t_1 + t_2) + 1 \right], \quad (4.8)$$

$$A_4 = \left[\frac{u_2\epsilon_1}{u_1\epsilon_2} \tan u_2 t_2 - \tan u_1 t_2 \right] \quad (4.9)$$

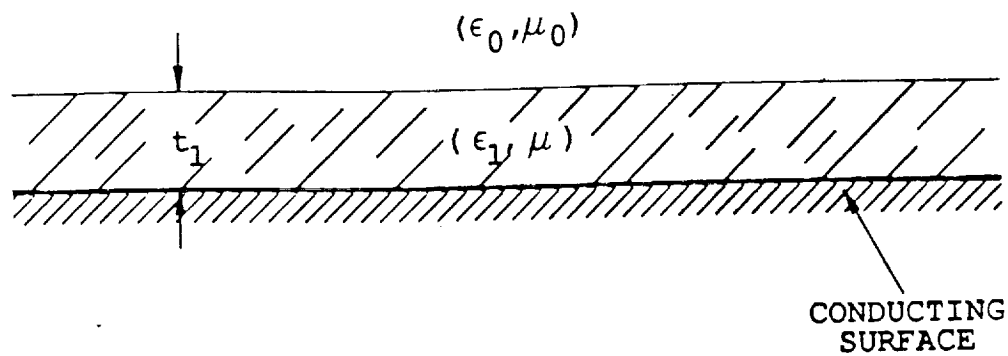
with $-v^2 - \gamma^2 = k_0^2$, $u_1^2 - \gamma^2 = k_1^2$ and $u_2^2 - \gamma^2 = k_2^2$. The wavenumbers k_i are given by $k_i = 2\pi f \sqrt{\epsilon_i \mu_0}$.

Typical plots for α and β are shown in Figures 4.3 through 4.5 as a function of frequency. The parameters for the single layer are $\epsilon_r = (2.54, -j0.)$ and $t = .125''$ and for the double layer are $\epsilon_{r1} = (2.54, -j0.)$, $\epsilon_{r2} = (30, -j5.)$, $t_1 = .125''$ and $t_2 = .015625''$. Note that there is a definite difference between the attenuation constants for the various configurations as a function of frequency. This functional difference may allow one to determine which model will more accurately describe the the coatings of interest.

The surface wave expression in Equation (4.1) is only appropriate when the separation distance between the probes is electrically large. More terms have to be added when the probes are not widely separated. In these cases, it is more convenient to calculate the coupling from a different approach. This other approach is commonly used in microstrip antenna applications and can be modified for this application [9]. Work in this area is presently being pursued.

An alternate technique for the determination of the dielectric constant

SINGLE LAYER



DOUBLE LAYER

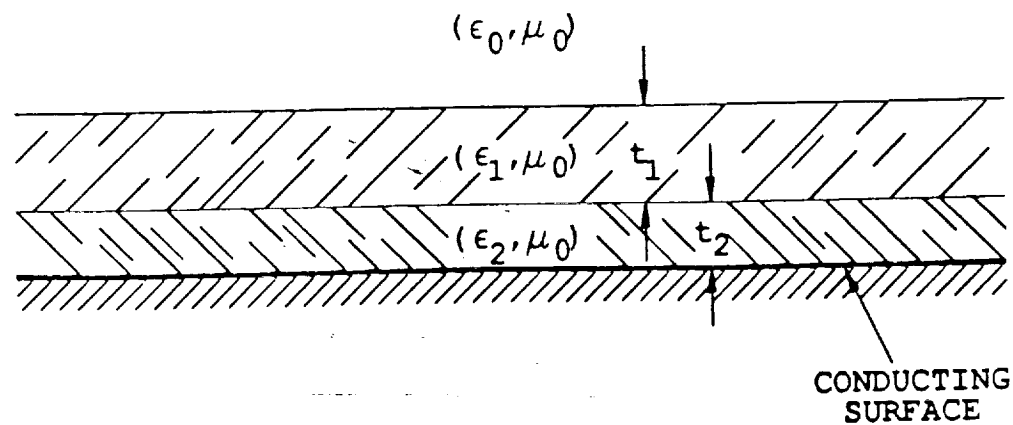


Figure 4.2: Analyzed geometry coatings for the dominant surface wave propagation constant.

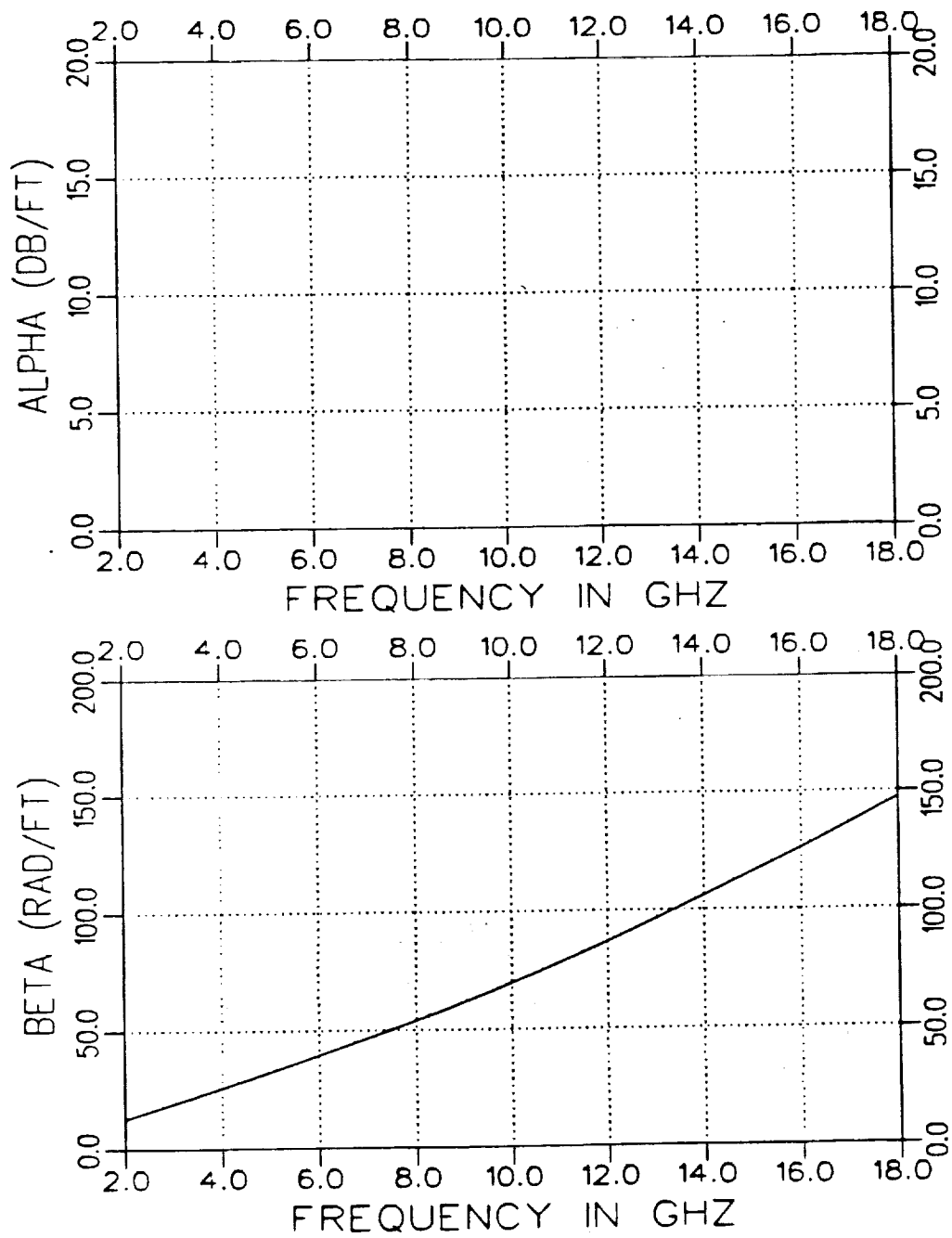


Figure 4.3: The attenuation and phase constant for a single layered coating where $\epsilon_r = (2.54, -j0.)$ and $t = .125''$ (negligible attenuation).

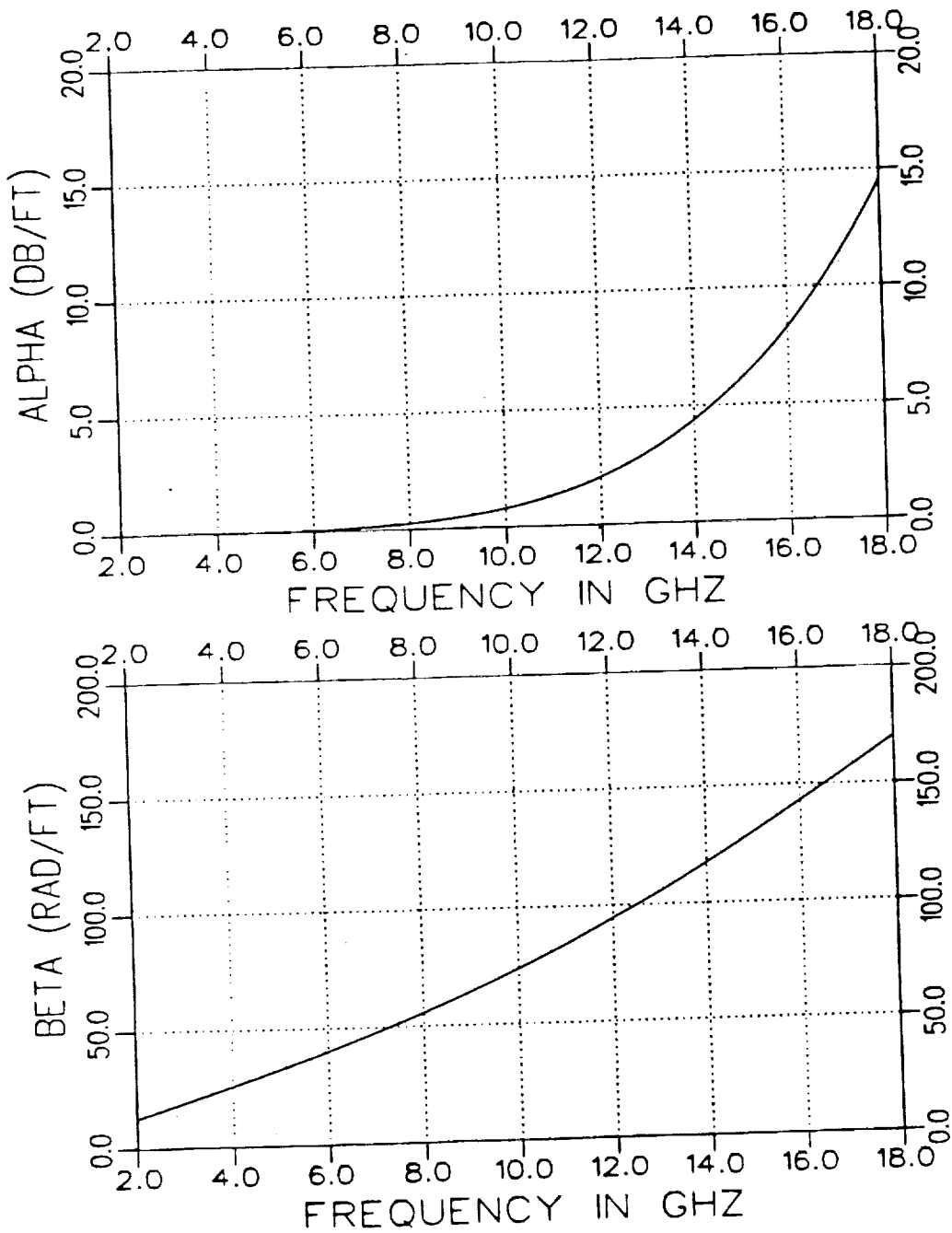


Figure 4.4: The attenuation and phase constant for a double layered coating where $\epsilon_{r1} = (30., -j5.)$, $\epsilon_{r2} = (2.54, -j0.)$, $t_1 = .125''$ and $t_2 = .015625''$.

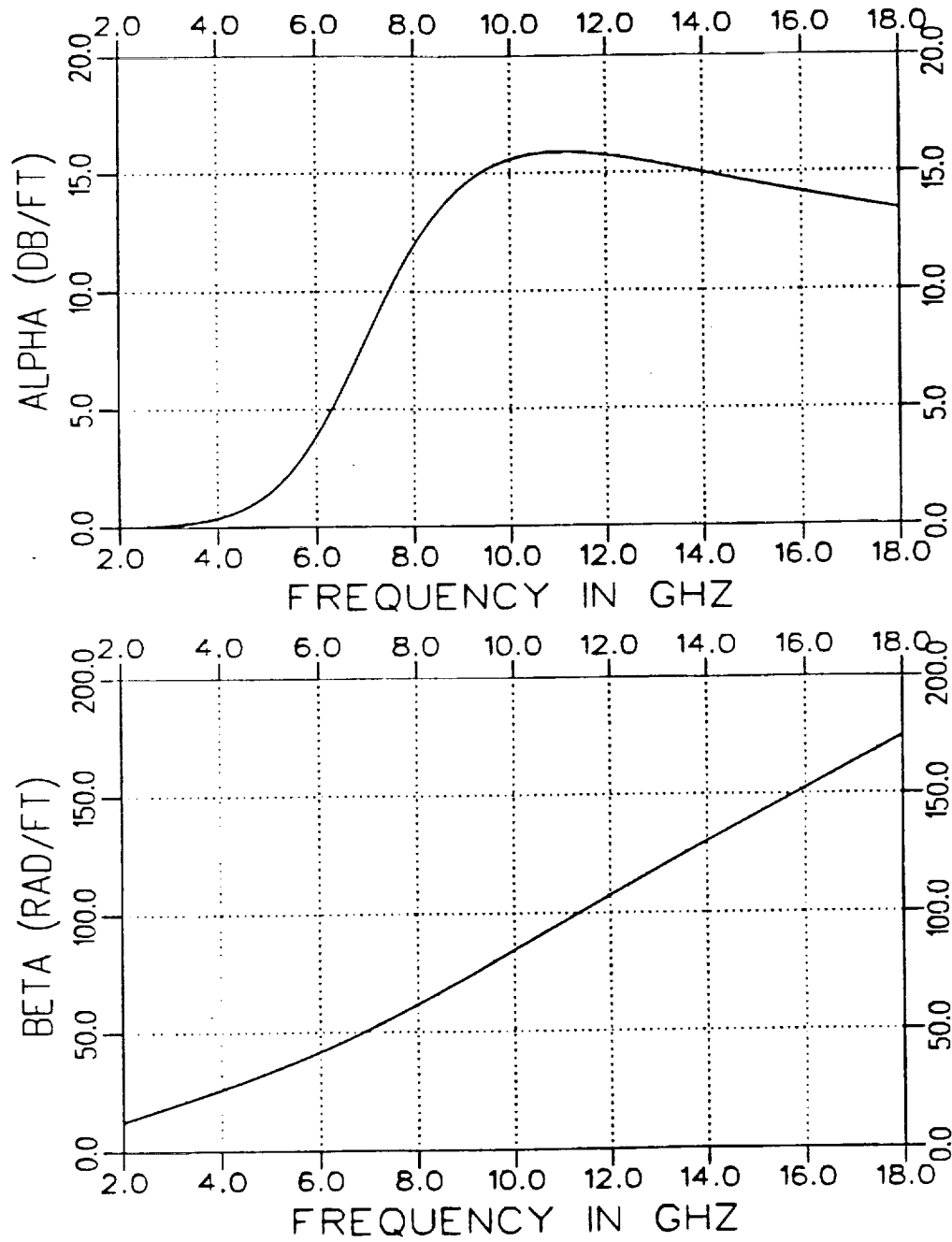


Figure 4.5: The attenuation and phase constant for a double layered coating where $\epsilon_{r1} = (30., -j5.)$, $\epsilon_{r2} = (2.54, -j0.)$, $t_1 = .015625''$ and $t_2 = .125''$.

would be to relate a probe's input impedance to the coating's dielectric constant. This approach will also be examined but it is believed that this parameter (input impedance) will not be as sensitive as the surface wave coupling. Experimentally, the input impedance can be obtained through a reflection measurement and analytically generated through a method of moments calculation [9].

Chapter 5

Conclusions

Calculations have indicated that material coatings are significant in modifying the electromagnetic scattering performance of untreated surfaces. The effort for the coming year will be a continuation of the tasks for the past year. The major tasks are outlined in the introduction and they are again:

- the electrical parameters of particular dielectric coatings,
- the scattered field characteristics due to these dielectric coatings,
- the measurement of the scattered field from these dielectric coatings in a metal chamber and
- the potential heating of these dielectric coatings from radio frequencies.

An additional topic of interest has formed from the need to classify the surface roughness for some of the material coatings. One application for this type of information occurs in calculating the scattered field from a rough surface. Knowledge of the roughness distribution can aid in a more accurate calculation since a uniform distribution is presently being used. A prototype system is being developed to satisfy this need.

The measurements performed at the ElectroScience Laboratory have aided in specifying the requirements necessary to achieve the experimental goals of this project. Much of the proper hardware has been purchased to assemble a measurement system for the measurement of the scattered fields from a dielectric coated surface in a metallic chamber.

Bibliography

- [1] D.R. Koberstein, "Near Field Synthetic Aperture Imaging of Probe Data for Scattering Studies of the ElectroScience Laboratory Compact Range," Report 718331-7, The Ohio State University ElectroScience Laboratory; Prepared under Contract GR9300, Boeing Aerospace Company, September 1986.
- [2] D.L. Mensa, *High Resolution Radar Imaging*, Dedham, MA, Artech House, 1981, pp. 103-118.
- [3] E.R. Walton and J.D. Young, "The Ohio State University Compact Radar Cross-Section Measurement Range," IEEE Trans. Antennas Propagat., Vol. AP-32, No. 11, pp. 1218-1223, November 1984.
- [4] K.M. Lambert and L. Peters, Jr., "Calculation of the effects of material on the backscatter of a ground plane," Report No. 720964-1, The Ohio State University ElectroScience Laboratory, Prepared under Grant NAG3-913, NASA Lewis Research Center, September, 1988.
- [5] R.J. Burkholder, "User Manual for LUMPS: Fortran Program for Calculating the RCS of a Random Array of Small Lumps Mounted on a Ground Plane," Report 720964-3, The Ohio State University ElectroScience Laboratory; Prepared under Grant NSG3 913, NASA Lewis Research Center, August 1989.
- [6] A.K. Dominek, H.T. Shamansky and R.M. Wood, "Backscatter from a Periodic Rough Surface at a Near Grazing Incidence," Report 716148-24, The Ohio State University ElectroScience Laboratory; Prepared under Grant NSG 1613, NASA Langley Research Center, October 1987.
- [7] R.F. Harrington, *Time Harmonic Electromagnetic Fields*, McGraw Hill Company, New York, NY, 1961.
- [8] J.A. Berrie and A.K. Dominek, "Surface Wave Characteristics in Layered Dielectric Coatings," Report 720964-4, The Ohio State University

ElectroScience Laboratory; Prepared under Grant NSG3 913, NASA Lewis Research Center, September 1989.

- [9] D.P. Forrai and E.H. Newman, "Radiation and Scattering From Loaded Microstrip Antennas Over A Wide Bandwidth," Technical Report No. 719493-1, The Ohio State University ElectroScience Laboratory; Prepared under Grant NSG 1613, NASA Langley Research Center, September 1988.